PHYSICAL REVIEW E **69**, 056305 (2004)

Dependence of turbulent Rayleigh-Taylor instability on initial perturbations

Guy Dimonte
Los Alamos National Laboratory, Los Alamos, New Mexico 87545, USA

(Received 6 October 2003; revised manuscript received 2 December 2003; published 19 May 2004)

The dependency of the self-similar Rayleigh-Taylor bubble acceleration constant α_b**(**$\equiv$[(amplitude)/2] $\times$(displacement)$\times$(Atwood number)**)** on the initial perturbation amplitude h_{0k} is described with a model in which the exponential growth of a small amplitude packet of modes makes a continuous nonlinear transition to its "terminal" bubble velocity $\propto$Fr [equal to (Froude number)$^{1/2}$]. Then, by applying self-similarity (diameter $\propto$ amplitude), α_b is found to increase proportional to Fr and logarithmically with h_{0k}. The model has two free parameters that are determined from experiments and simulations. The augmentation of long wavelength perturbations by mode coupling is also evaluated. This is found to decrease the sensitivity of α_b on the initial perturbations when they are smaller than the saturation amplitude of the most unstable modes. These results show that α_b can vary by a factor of 2–3 with initial conditions in reasonable agreement with experiments and simulations.

DOI: 10.1103/PhysRevE.69.056305 PACS number(s): 47.20.Bp

I. INTRODUCTION

The Rayleigh-Taylor (RT) instability [1,2] occurs when a fluid of density ρ_l accelerates another fluid of density $\rho_h > \rho_l$. If the unstable perturbations are broadband in wave number k and attain large amplitudes $h_k > 1/k$, the instability evolves self-similarly such that the dominant wavelength grows with the amplitude. Then, for a constant acceleration g, the light fluid penetrates the heavy fluid as bubbles with amplitude [3–29]

$$h_b = \alpha_b A g t^2, \tag{1}$$

where $A=(\rho_h-\rho_l)/(\rho_h+\rho_l)$ is the Atwood number. Experiments [7–14] with immiscible liquids obtain $\alpha_b \sim 0.04-0.07$ whereas numerical simulations (NS) initialized with only short wavelength perturbations [15,16,29] obtain $\alpha_b \sim 0.03$. Glimm *et al.* [17] obtain a larger value $\alpha_b \sim 0.05$ that increases to 0.08 when front-tracking (FT) is employed thereby suggesting that numerical diffusion could reduce α_b. However, other NS with FT [18] obtain $\alpha_b \sim 0.05$ and NS [29] with and without interface reconstruction (IR) obtain $\alpha_b \sim 0.03$ because the fluid entrainment with IR is found to be similar to the numerical diffusion without IR. Thus the numerics may not be responsible for all of the differences in α_b. For example, α_b may depend on the initial conditions [3–6,11,14,19,27] since NS [11] show that adding an initial long wavelength component as small as 0.01λ can double α_b.

A strict analytical theory for α_b is not yet available to clarify these issues, but Eq. (1) can be obtained by combining the two key characteristics of RT bubbles, namely, that (1) their characteristic velocity is proportional to that of a single bubble [30–50]

$$\mathrm{V}_b = \mathrm{Fr}\sqrt{\frac{\delta\rho}{\rho_h}\frac{gD_b}{2}} \tag{2}$$

and (2) their diameter grows self-similarly $D_b \propto h_b$. Then, Eq. (2) yields Eq. (1) with

$$\alpha_b = \frac{\mathrm{Fr}^2}{8}\frac{\Sigma\rho}{\rho_h}\frac{D_b}{h_b}, \tag{3}$$

where $\delta\rho \equiv \rho_h - \rho_l$, $\Sigma\rho \equiv \rho_h + \rho_l$ and Fr is a constant equal to (Froude number)$^{1/2}$. For $A=1$, potential flow models and experiments yield $\mathrm{Fr} \sim 0.5$ for a bubble in a cylinder [30–34,37] and $\mathrm{Fr} \sim 2/3$ for a lenticular bubble in an infinite fluid [31,36]. For $A<1$, Eq. (2) can be obtained by equating buoyancy $(\delta\rho g)$ and drag $(C_d \rho_h V_b^2/D_b)$ forces such that $\mathrm{Fr} \propto 1/\sqrt{C_d}$ [26,30,40]. In general, Fr depends on the shape and environment of the bubble since they form the streamlines in the heavy fluid [31,32,36]. These issues are discussed further in in Secs. II and III.

The more complex and unresolved issue is associated with the self-similar evolution of the bubbles to successively longer wavelength. This can proceed in two limiting ways, namely, by (1) the nonlinear coupling of saturated shorter wavelength modes, or (2) the exponential amplification and saturation of ambient modes.

The first mechanism is invoked in bubble merger models [21–26,18] and leads to an α_b that depends primarily on the merger rate since it determines D_b/h_b in Eq. (3). Since the mode-coupling or merger process is nonlinear and involves saturated modes of intrinsic scales $(h_k \sim 1/k)$, the associated α_b is insensitive to the initial conditions and perhaps universal. However, if one uses the observed $D_b/h_b \sim 0.55\rho_h/\Sigma\rho$ [13,14] and $\mathrm{Fr} \sim 1/\sqrt{\pi}$ for a periodic array, then Eq. (3) yields $\alpha_b \sim 0.022$, which is smaller than observed. In the second process, the longer wavelength modes are produced by the unstable amplification and nonlinear saturation of the initial perturbations. Since the linear growth is exponential, α_b may depend logarithmically on the initial conditions [3–6,11,14,19,27] but the dependence has not yet been quantified.

In this paper, the effect of initial conditions on α_b is evaluated quantitatively using simple model calculations. The model has two free parameters that are determined by comparing the results with published experiments and NS. It is important to clarify these issues quantitatively because so-called “mix models” [8,21–26,51–59] are calibrated with α_b.

The dependence of α_b on the initial perturbations is obtained from known single mode dynamics, namely, by melding the classical RT exponential growth at small amplitude to the terminal bubble velocity at large amplitude. To preserve continuity in amplitude and growth rate, the nonlinear transition (attributed to Fermi in Ref. [32] is taken to be when the linear velocity equals the terminal velocity and this occurs near $h_k \sim 1/k$ when the growth rate is classical $\Gamma \sim \sqrt{Akg}$. The resulting equations are similar in form to those introduced by Birkhoff [3] and extended by Cherfils and Mikaelian [4] for single modes. However, in the turbulent RT instability, the wave spectrum is broad and nearby modes can interfere constructively as described by Haan [51,52]. As a result, nonlinear saturation occurs when the root-mean-square (rms) amplitude of the wave packet is comparable to its average wavelength and the saturation amplitude of the individual components are reduced by a phase-space factor to $h_k \sim 1/k^2L$ in three dimensions (3D), where L is the system width. Such a suppression in a multimode system was observed directly in the beam-plasma instability [60,61]. More importantly, the rms amplitude of the multimode wave packet was found to evolve into the nonlinear regime just like a single mode until the beam electrons resolved the spectral width. This implies that bubbles with a spectral width δk can be represented on a rms basis as a single dominant bubble for an autocorrelation time $\propto 1/V_b\delta k$ after saturation. This approach is used here to adapt Birkhoff’s solution for individual modes to the bubble wavepacket, and for arbitrary A and initial perturbation spectra. Then, by invoking self-similarity, we obtain α_b and D_b/h_b in terms of the initial perturbations and Fr. Fr is then obtained by analyzing images of RT bubbles in the linear electric motor (LEM) experiments [12–14]. The initial amplitudes on the LEM are inferred from early-time images taken with laser induced fluorescence (LIF).

The augmentation of the long wavelength perturbations due to mode coupling is also evaluated in Sec. V by applying Haan’s analysis [52] to describe the nonlinear production of long wavelength $\sim L$ modes by the most unstable modes. The mode coupling component is then added in quadrature [52] to the amplified ambient perturbations to obtain an α_b that spans the two limiting regimes. As expected, α_b is found to be insensitive to the initial conditions when the ambient long wavelength modes are smaller than the saturation amplitude of the most unstable modes. Coincidentally, many published NS [16–20] are initialized with such perturbations and the present model is able to describe their results. Mode coupling is found to have a minor effect for relatively large and broadband initial perturbations. It should be pointed out that the mode-coupling contribution described here is not a general theory of mode coupling since it does not describe the usual progression to longer wavelength by a cascading process. The latter is done better by the merger models [21–26,18].

Please note that this paper considers only 3D perturbations with a total wave number $k=\sqrt{k_x^2+k_y^2}$ where k_x and k_y are the components in two directions transverse to $g\hat{z}$.

II. BASIC MODEL

The basic model is obtained by adapting the evolution of a single-mode to a multimode wave packet centered at the wave number of the dominant bubble. The single-mode solution [3] grows exponentially at small amplitude and with the terminal bubble velocity at large amplitude. As was done successfully in the beam-plasma instability [60,61], the single-mode solution is attributed to the root-mean-square (rms) amplitude of a multimode bubble wave packet [51] but with an evolving dominant wavelength [3] for the RT instability.

A. Single-mode solution

At small amplitude $kh_k \ll 1$, it is well known that RT unstable perturbations grow as

$$h_k = h_{0k}\cosh(\Gamma t). \tag{4}$$

If the number of e-foldings is $\Gamma t \geqslant 2.3$ (amplification $\geqslant 10$), Eq. (4) can be represented by

$$h_k \sim \frac{h_{0k}}{2}\exp(\Gamma t), \tag{5}$$

with $<1\%$ error and this simplifies the algebra.

Generally, the linear growth rate is $\Gamma \sim \sqrt{Akg}$ at low k and is limited by various microscopic processes at high k [62]. For example, liquids with an interfacial surface tension σ have

$$\Gamma = \sqrt{Akg - \frac{\sigma k^3}{\rho_l + \rho_h}}, \tag{6}$$

which has a peak value $\Gamma \sim 0.82\sqrt{Ak_pg}$ at wave number $k_p = \sqrt{\delta\rho g/3\sigma}$. Fluids with a viscosity ν have a peak growth rate of $\Gamma \sim 0.71\sqrt{Ak_pg}$ at $k_p \sim 0.5(Ag/\nu^2)^{1/3}$. ln ICF, ablation at the capsule surface produces an outward stabilizing flow [63,64] with velocity v_a and a peak growth rate $\Gamma \sim 0.5\sqrt{k_pg}$ at $k_p \sim 0.1g/v_a^2$. Modes with $k > 2–3\ k_p$ are stabilized fully by surface tension and ablation flow, but only partially by viscosity because the viscous retarding force requires a finite velocity $\sim \Gamma h_k$. Eventually, modes with $k < k_p$ will dominate and their growth rate is $\Gamma \sim \sqrt{Akg}$.

At large amplitude, a single (or periodic) bubble attains a terminal velocity that increases with A. For $A=1$, Hecht, Alon and Shvarts [34] extended Layzer’s potential flow model [33] to a square periodic bubble array ($k_x=k_y$) and obtained

$$\frac{dh_b}{dt} = \sqrt{\frac{g}{k}} \sim 0.56\sqrt{\frac{g\lambda}{2}}. \tag{7}$$

Their result is equivalent to Layzer’s Fr~ 0.51 for a bubble in a cylinder with radius $R=3.83/k$ (3.83 is first zero of Bessel function J_0). Goncharov [40] extended this analysis to $A<1$ and obtained

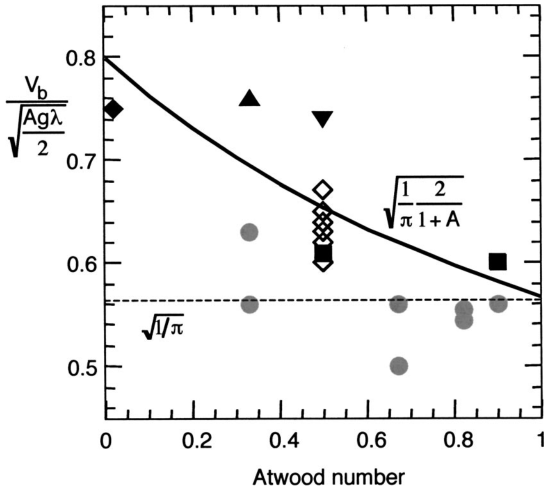

FIG. 1. Scaled bubble terminal velocity for a single 3D mode vs Atwood number. The solid line represents Eq. (8) and the dashed line is Eq. (9). Points are taken from the following publications: ◆, Trygvasson and Unverdi [42]; ●, Li [43,44]; ▼, Hecht [45]; ■, He [46]; ◇, Calder [47]; ◇, Alpha group [26].

$$\frac{dh_b}{dt} \sim 1.02\sqrt{\frac{2A}{1+A}\frac{g}{k}} \sim 0.58\sqrt{\frac{2A}{1+A}\frac{g\lambda}{2}}, \tag{8}$$

which is consistent with Eq. (2) and a buoyancy-drag model [26] if $D_b \sim \lambda$. Sohn [41] assumed a different potential in the light fluid and obtained

$$\frac{dh_b}{dt} \sim C\sqrt{\frac{Ag\lambda}{2}}, \tag{9}$$

which is consistent with Eq. (2) if $D_b \sim \lambda(1+A)/2$. It is also similar to the scaling suggested by Glimm and Li [21] and in numerical single studies [45–47]. Both Eqs. (8) and (9) have the same limiting values at $A=0$ and 1, but potential flow ignores the vortical motion surrounding the bubble at $A \ll 1$ and this may affect the Atwood dependence. In particular, it is surprising that both Goncharov [40] and Sohn [41] find the radius of curvature to be independent of A, namely, $3.35/k$ and $4/k$, respectively.

A comparison of Eqs. (8) and (9) with published 3D simulations seems to favor Eq. (8) but not conclusively. In Fig. 1, the scaled velocity $V_b/\sqrt{Ag\lambda/2}$ from the simulations (points) seems to decrease with A as suggested by Eq. (8). Analogous agreement with Eq. (8) in 2D was reported by Alon. *et al.* [26] and Mikaelian [42]. However, there is considerable scatter in the simulations and there is some ambiguity between D_b and λ. For example, 2D simulations by Daly [65] found that

$$\lambda \sim D_b\frac{\Sigma\rho}{\rho_h} = D_b\frac{2}{1+A}, \tag{10}$$

which is physically reasonable since the spikes are very narrow at $A=1$ so that $\lambda \sim D_b$ and they are identical to bubbles at $A=0$ so that $\lambda \sim 2D_b$. This is inconsistent with 3D potential flow calculations [40,41] that obtain $\lambda \sim D_b$ independent of A.

Given these ambiguities, the bubble velocity is taken to have the form of Eq. (9) in developing the present model, but C is a free parameter and is related to Fr as follows:

$$C = \mathrm{Fr}\sqrt{\frac{\Sigma\rho}{\rho_h}\frac{D_b}{\lambda}} = \mathrm{Fr}\sqrt{\frac{2}{1+A}\frac{D_b}{\lambda}}. \tag{11}$$

As indicated previously, Eq. (2) leads to Eq. (9) if $D_b \sim \lambda\rho_h/\Sigma\rho$ and Eq. (8) if $D_b \sim \lambda$. This will be discussed further in Secs. III and IV.

The linear and nonlinear single-mode solutions are then combined simply by making a transition between them when the linear velocity Γh_k equals the bubble velocity. This is attributed to Fermi and occurs when

$$C\sqrt{\frac{Ag\lambda}{2}} \sim \Gamma h_k \sim \frac{\Gamma h_{0k}}{2}\exp(\Gamma t_{\mathrm{NL}}) \tag{12}$$

at a time

$$t_{\mathrm{NL}} \sim \frac{1}{\Gamma}\ln\left(\frac{2C}{\Gamma h_{0k}}\sqrt{\frac{Ag\lambda}{2}}\right). \tag{13}$$

At $t=t_{\mathrm{NL}}$, the solution transitions from Eq. (4) to

$$h_k = C\sqrt{\frac{Ag\lambda}{2}}\left[\frac{1}{\Gamma} + t - t_{\mathrm{NL}}\right]. \tag{14}$$

This is similar to the solution of Birkhoff [3] and Cherfils and Mikaelian [4]. As shown in Fig. 2, it also agrees with a single-mode 3D simulation by Weber in the Alpha group Collaboration [29] with 32 zones/λ on each side and $h_{0k} = 0.001\lambda$. The linear growth rate is nearly classical $\Gamma \sim 0.95\sqrt{Akg}$ limited by numerical dissipation and the terminal velocity is $V_b = 1.34$ cm/s corresponding to $C \sim 0.6$. The model solution (dashed line) fits the simulation results within <1 % in the linear regime and within 21% in the nonlinear regime similar to that in Refs. [32,42]. The worst agreement occurs near the transition at $t=8$ s when the amplitude is 1.72 cm in the simulations and $\delta h_k \sim 0.36$ cm larger in the model. The model amplitude is 21% larger because the simulation begins the transition about one *e*-folding before t_{NL} and then approaches V_b more gradually. This also seen in Fig. 9 of Ref. [48]. However, as we shall see below, this mode is expected to dominate when $h_k \sim 2\lambda$ and the discrepancy $\delta h_k \sim 0.41$ cm is $\delta h_k/h_k < 3\%$, which is smaller than the ±5% scatter in C exhibited in the simulations in Fig. 1.

B. Multimode bubble wave packet

It is now possible to describe the broadband (RT) instability by applying the single-mode solution to the (bubble) wave packet of modes centered at the dominant wavelength as suggested by DeNeef [60] for the beam-plasma instability and Haan [51] for the RT instability. In the beam-plasma instability, a single mode grows exponentially until its amplitude is large enough to trap the beam electrons and then the amplitude oscillates as the electrons slosh in the sinusoidal potential. When experiments were repeated with a finite band of modes [60,61], it was found that the *total wave*

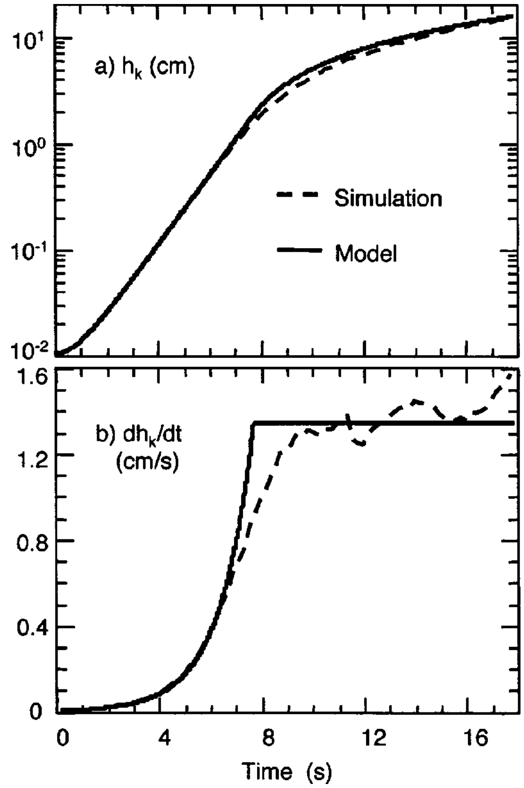

FIG. 2. (a) Amplitude and (b) velocity for a 3D single mode with $A=0.5$, $g=2$ cm/s^2, and $\lambda=10$ cm. The solid line from simulations by Weber in Ref. [26] and the dashed line given by Eqs. (4) and (14) with $\Gamma=0.95\sqrt{Akg}$ and $C=0.6$.

energy (*modes added in quadrature*) *evolved identically to that of a single mode* until the electrons resolved the spectral spread, namely, for an autocorrelation time after saturation. For the broadband RT instability, Haan [51,52] made the similar argument that saturation occurs when the overall amplitude of the entire band of dominant modes becomes comparable to their average wavelength. The idea is that modes within this bubble wave packet can interfere constructively to produce a net amplitude that greatly exceeds the individual modal amplitudes. In both cases, the hypothesis is that the rms amplitude of a multimode wave packet

$$\langle h_k\rangle \equiv \left[\frac{L^2}{2\pi}\int_{k-\delta k}^{k+\delta k} dk' k' h_{k'}^2\right]^{1/2} \tag{15}$$

evolves similarly to the single mode solution for some autocorrelation time into the nonlinear regime. Thus saturation occurs when $\langle h_k\rangle$ becomes comparable to the dominant wavelength, but the individual mode amplitudes are smaller by the phase space factor kL in 3D, i.e., $h_k\propto 1/k^2L$ This suppression was observed directly in the beam-plasma instability [60,61].

The effective width of the wave packet δk will be estimated in Sec. III B, but it is first useful to review the expected evolution of an RT unstable spectrum. This is shown schematically in Fig. 3 for a $1/k^2$ initial spectrum and two times. The nonlinear modes are those that exceed the Haan saturation amplitude $h_k\propto 1/k^2L$ (dashed line) and these have $k>k_s$. Bubbles are associated with the spectral peak at k_b with amplitude $h_b=\langle h_k\rangle$. At the early time t_1, the bubbles are comprised of the fastest growing waves $k_b\sim k_p$. As time increases to t_2, slower-growing longer-wavelength modes overtake the initially saturated modes and all scales $1/k_s$, $1/k_b$ and h_b grow self-similarly. In this picture, the wave packet is comprised of the dominant bubbles that have just become nonlinear with an effective width $\delta k\propto k_b-k_s$.

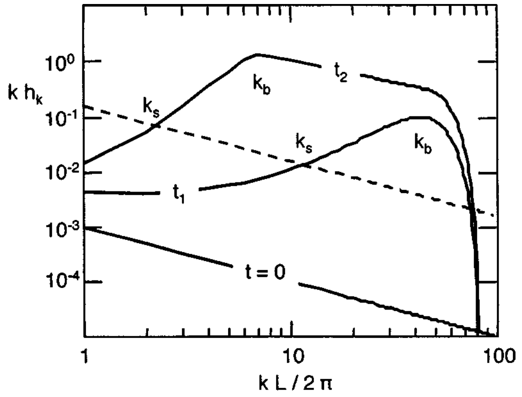

FIG. 3. Schematic representation of the perturbation spectrum at various times $0<t_1<t_2$. Dominant bubbles have wave number k_b and modes saturate at k_s when they exceed the Haan saturation amplitude Eq. (25) (dashed line).

Within this picture, the single mode solution in Sec. II A is adapted to the multimode RT instability by assigning $h_b=\langle h_k\rangle$. Then, the Fermi transition is applied to the wave packet $\langle h_k\rangle$ by equating the linear and nonlinear velocities

$$\Gamma h_b = C\sqrt{\frac{Ag\lambda_b}{2}}. \tag{16}$$

The fastest growing modes $k\sim k_p$ will saturate first and they have $\Gamma<\sqrt{Akg}$, but the longer wavelength modes $k<k_p$ that dominate the later stages have a nearly classical growth rate $\Gamma\sim\sqrt{Akg}$. The classical modes transition at an amplitude

$$k_b h_b = k_b\langle h_k\rangle \sim C\sqrt{\pi} \tag{17}$$

and a time

$$t_{\mathrm{NL}} \sim \frac{1}{\sqrt{Ak_b g}}\ln\left(\frac{2C\sqrt{\pi}}{k_b\langle h_{0k}\rangle}\right). \tag{18}$$

For $t\geqslant t_b$, the solution to Eq. (9) can then be written as

$$h_b = C\sqrt{\pi}\left[\frac{1}{k_b}+\sqrt{\frac{Ag}{k_b}}(t-t_{\mathrm{NL}})\right]. \tag{19}$$

The evolution of h_b is exemplified for constant mode numbers $n=kL/2\pi$ by the dashed lines in Figs. 4(a) and 4(b) for $k\langle h_{0k}\rangle=10^{-6}$ and 10^{-3}, $\mathrm{Fr}=2/3$ and $A=1$. Each mode transitions from an initial exponential growth to a terminal velocity with a continuous slope at t_{NL} indicated by solid points. A key finding is that the envelope (thick solid line) obeys Eq. (1) as fast growing high-k modes saturate and are overtaken by slower growing low-k modes. (Please

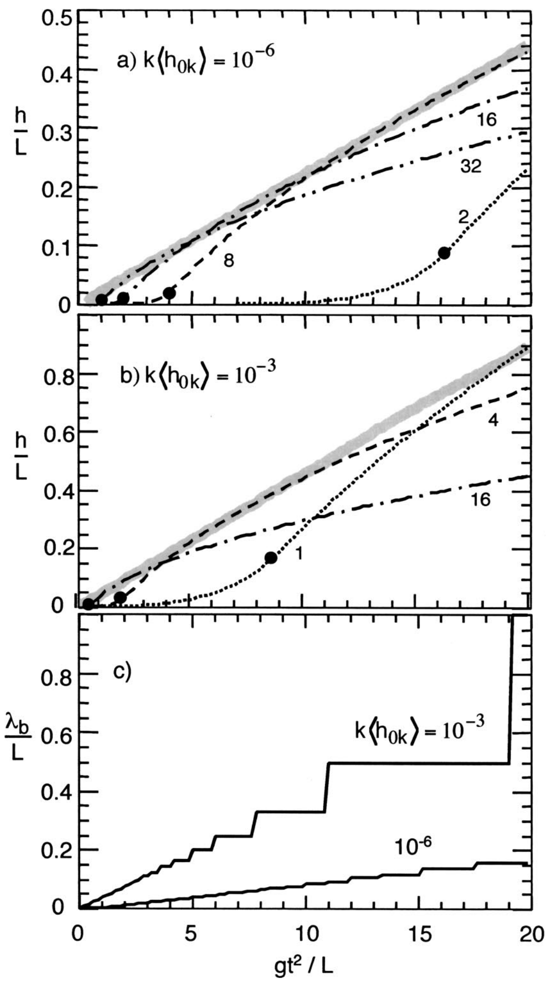

FIG. 4. Scaled solutions to Eq. (10) (broken lines) for $A=1$ and $k\langle h_{0k}\rangle=10^{-6}$ (a) and 10^{-3} (b). The envelope of modes (gray solid line) follows Eq. (1). (c) Wavelength of the dominant mode that comprises the envelope.

note that when a mode n is the dominant mode, the mode $n/4$ has just become nonlinear as indicated by the points.) Thus, Eq. (1) can be thought of as a nonlinear progression to successively longer wavelength packets or like a competition of noninteracting bubbles. This process results in a self-similar evolution as seen in Fig. 4(c) since the wavelength of the dominant bubble λ_b also increases as gt^2. It is noteworthy that the dependence on $\langle h_{0k}\rangle$ is weak since $\alpha_b \sim 0.022$ and $\lambda_b/h_b \sim 0.36$ at $k\langle h_{0k}\rangle=10^{-6}$ and $\alpha_b \sim 0.045$ and $\lambda_b/h_b \sim 1.12$ at $k\langle h_{0k}\rangle=10^{-3}$.

Following Birkhoff [3], the self-similar evolution of the dominant bubbles can be obtained by seeking the wavelength that maximizes Eq. (19). This is done by setting

$$\frac{\partial h_b}{\partial \lambda_b} \sim \frac{C}{2\sqrt{\pi}}\left[\sqrt{\frac{Ag}{2\lambda_b}}t + 1 - \ln\left(\frac{C\sqrt{\pi}}{k_b\langle h_{0k}\rangle}\right)\right] = 0, \qquad (20)$$

assuming that $h_{0k} \sim k^{-2}$ because that makes $k\langle h_{0k}\rangle$ independent of k. The solution to Eq. (20) is

$$\lambda_b \sim \frac{\pi A g t^2}{2\left[\ln\left(\frac{2C\sqrt{\pi}}{k_b\langle h_{0k}\rangle}\right) - 1\right]^2}. \qquad (21)$$

Inserting Eq. (21) into Eq. (19) yields Eq. (1) with

$$\alpha_b \sim \frac{C\sqrt{\pi}}{4}\left[\ln\left(\frac{2C\sqrt{\pi}}{k_b\langle h_{0k}\rangle}\right) - 1\right]^{-1} \qquad (22)$$

and a self-similarity ratio

$$\beta_b \equiv \frac{\lambda_b}{h_b} \sim \frac{2\sqrt{\pi}}{C}\left[\ln\left(\frac{2C\sqrt{\pi}}{k_b\langle h_{0k}\rangle}\right) - 1\right]^{-1}. \qquad (23)$$

This analysis extends that of Birkhoff in two simple ways. First, Birkhoff considered only $A=1$ since the nonlinear solution was obtained from potential flow whereas this is extended to $A<1$ based a buoyancy-drag description. Second, Birkhoff [3] ascribed the solution to individual modes and assumed that $h_{0k} \sim k^{-1}$ to keep kh_{0k} constant. Here, the solution is ascribed to the bubble envelope in an rms sense and $k\langle h_{0k}\rangle$ is constant only when $h_{0k} \sim k^{-2}$ as suggested by Inogamov [5,6]. However, to his credit, Birkhoff appears to be the first to have predicted the self-similar behavior embodied in Eqs. (1), (22), and (23), and based on what was thought to be practical $kh_{0k} \sim 10^{-3}$, he predicted an $\alpha_b \sim 0.12$ and $\beta_b \sim 1$ close to what was measured decades later.

However, in general, α_b and β_b can depend on $k\langle h_{0k}\rangle$ as exemplified in Fig. 5 from Eqs. (22) and (23) for $C=0.56$ and 0.95. The behavior can be understood by noting that the dominant modes are those just beyond saturation. Since the time to saturation t_{NL} decreases as the initial amplitude increases, α_b and β_b increase with $\langle h_{0k}\rangle$, but only logarithmically because the initial growth is exponential. α_b increases with C because it increases the terminal velocity but β_b decreases with C because a mode must be amplified further to reach the larger terminal velocity. Please note that inertia $\ddot{h}_b$ is neglected when applying self-similarity or bubble merger to a constant terminal velocity, but the associated error in Eq. (22) is $2\alpha_b \sim 10\,\%$.

III. MODEL CONSTANTS

The model has two unknown constants C and ε_b. The two output parameters vary as $\alpha_b \propto C$ and $\beta_b \propto 1/C$ and increase logarithmically with ε_b. Physically, C is related to Fr by Eq. (11) and determines the bubble "terminal" velocity. In this model, it also absorbs possible uncertainties in the transition between the linear and nonlinear solutions. The relative spectral width ε_b defines the spectral content of the bubbles and is used to relate the bubble rms mplitude to the initial Fourier spectrum of the perturbations.

A. Bubble velocity $\propto C$

The value of $C \sim 0.95$ required to describe the LEM results (Sec. IV) is larger than the classic result of $\text{Fr} \sim 0.5$ for a single bubble in a tube with $A=1$ [30–32] but it is compa-

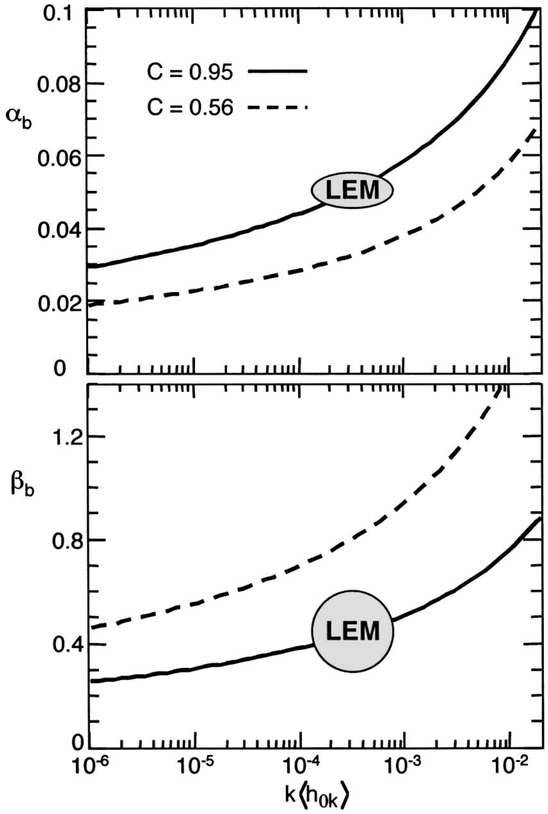

FIG. 5. Variation of α_b and β_b with $k\langle h_{0k}\rangle$ from Eqs. (13) and (14) for $C=0.95$ (solid lines) and 0.56 (dashed lines). Ellipses signify LEM results.

rable to Fr ~ 1 obtained for RT bubbles [43,21,22,14] and Fr ~ 1.2 for plumes [35]. This was first pointed out by Lewis [43] and clarified further by Glimm and collaborators [21–24]. The uncertainty arises because the velocity of a bubble is determined by its shape and environment [32,35] since they form the streamlines of the flow and they are complex in the chaotic RT bubble front.

The two classic configurations cited in the RT literature are shown in Fig. 6: (a) long columnar bubble bounded in a cylinder of diameter D and (b) a short lenticular bubble in an extended fluid. The shape of a bubble is approximated by its radius of curvature near the apex R_c and its vertical extent L_b. The environment is characterized by the area around the bubble that accommodates the counterflow of the "heavy" fluid. Namely, to counter the upward flow of the bubble, the downward velocity of the displaced "heavy" fluid (and drag) is larger for a bounded bubble than for an unbounded bubble because the surrounding area is smaller.

The scaled velocities for individual bubbles are summarized in Table I. Experiments and potential flow calculations yield a velocity $0.5\sqrt{gD/2}$ for a bubble bounded in a cylinder and $0.67\sqrt{gR_c}$ for an unbounded lenticular bubble. Collins [36] consolidated these results by considering the effect of a cylindrical boundary of arbitrary $D/2R_c$. For the bounded bubble, the cylinder is found to deform the bubble so that $R_c\sim 1.04\mathrm{D}/2$ and Fr ~ 0.51. For the unbounded bubble, he uses the last closed circular streamline to define an effective sphere for the lenticular bubble with $D_b\sim 2R_c$ and obtains Fr ~ 2/3 similar to Davies and Taylor [31].

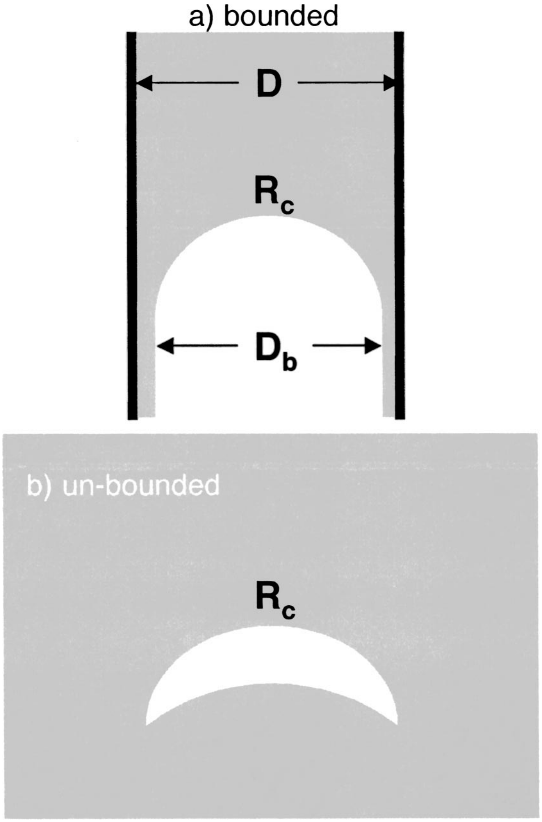

FIG. 6. Schematic of (a) a bubble bounded in a cylinder and (b) a lenticular bubble in an extended fluid.

For individual RT bubbles, the scaled velocities were measured to be 0.7–1.2 [21,22,14] similar to that for plumes ~1.2 [35]. Indeed, by comparing the images in Figs. 1–3 of Ref. [35] and Fig. 11 in Sec. IV, one sees that plumes and RT bubbles appear to be long and unbounded. And both features tend to increase Fr. The importance of the length can be understood from the drag constant of an ellipsoid of revolution [66], which yields an $\mathrm{Fr}\propto L_b/D_b$. Of course, this is intuitively clear to those who draft behind vehicles in bicycle and automobile races.

The RT bubble front has been approximated by a square periodic lattice of bubbles. As seen in Table II, potential flow calculations reproduce the results ($R_c\sim 1.04D/2$ and Fr ~ 0.51 of Collins for a bounded bubble if $\lambda_b\sim D$ and 3D simulations obtain slightly higher values of Fr ~ 0.5–0.74. However, a perfectly periodic configuration is not an accurate representation of a chaotic RT bubble front since it underestimates Fr and thus α_b.

This discrepancy may by due to the unstable nature of a uniform periodic lattice [21–24]. For example, suppose that bubbles 2 and 4 in the uniform front (solid) in Fig. 7 are perturbed forward slightly. These bubbles may experience a smaller counterflow of the "heavy" fluid like an unbounded bubble and the reduced drag will further increase their velocity ahead of their neighbors. To quantify this effect, Glimm and Li [21] suggested a superposition hypothesis in which "the effective bubble velocity is the sum of the single bubble velocity and the single bubble velocity of the envelope." For example, if the chaotic bubble front is modulated

TABLE I. Scaled bubble velocity from single-mode experiments, potential flow models and 3D numerical simulations, and in RT experiments.

	A	$\frac{V_b}{\sqrt{gD/2}}$	$\frac{V_b}{\sqrt{gR_c}}$	$\frac{V_b}{\sqrt{g.5D_b\delta\rho/\rho_h}}$
Bubble in cylinder				
Experiment [30]	1	0.48		
Potential flow [30]	1	0.49		
Experiment [31]	1	0.48		
Potential flow [31]	1	0.46		
Potential flow [32]	1	0.51		
Potential flow [36]	1	0.5	0.51	
Bubble in large bath				
Lenticular bubbles [31]	1		0.67	
Potential flow [36]	1		0.65	
Plumes [35]	$\ll 1$			1.2
Bubbles in RT experiments				
Lewis [43]	1			1.1
"Rocket rig" [7,8,21–24]	0.5–0.99			0.7–1.2
LEM [13,14]	0.2–0.96			0.7–1.0

at $2\lambda_b$ as shown in Fig. 7, the hypothesis suggests that the leading bubble velocity is augmented by $\sqrt{2}$ to that observed $\mathrm{Fr} \sim 0.51(1+\sqrt{2}) \sim 1.2$. Cheng, Glimm and Sharp [24] extended this analysis to 3D and obtained $\alpha_b \sim 0.05-0.06$ and $D_b/h_b \sim 1/3$ independent of A. However, rather than invoking bubble interactions, the leading RT bubbles may simply behave like plumes in an extended bath and they have Fr ~ 1 because they are unbounded and long vertically [66].

Independent of this model, it is important to have $\mathrm{Fr} \sim 1$ because then Eq. (3) yields $\alpha_b \sim 0.06$ for the observed $D_b/h_b \sim 0.5\rho_h/\Sigma\rho$ [Fig. 13(b)] instead of $\alpha_b \sim 0.024$ for Fr ~ 0.56. Oron *et al.* [18] increased α_b by increasing the bubble merger rate so that $\lambda_b/h_b \sim 1$, but this is 2–3 times larger than observed in Fig. 13(b). Cheng, Glimm and Sharp [24] were able to obtain $\alpha_b \sim 0.05-0.06$ with $D_b/h_b \sim 1/3$ by invoking an envelope instability for a chaotic bubble array.

B. Bubble spectral width $\propto \varepsilon_b$

The model in Sec. II depends primarily on C if written in terms of the bubble h_b or rms amplitudes $\langle h_k \rangle$. However, in order to calculate $\langle h_{0k} \rangle$ from the spectral amplitudes h_{0k}, such as from an ICF capsule or a simulation, it is first necessary to obtain the effective spectral width δk for the integral in Eq. (15). This can be done by defining a second free parameter

$$\varepsilon_b = \delta k/k \tag{24}$$

that describes the spectral width of the dominant bubbles. In the following, we estimate $\varepsilon_b \sim 3/8$ and this is similar to the effective spectral width obtained in the bubble merger model [Fig. 6(c)] of Oron *et al.* [18]. In any case, the model results are not very sensitive to ε_b because α_b and β_b depend only logarithmically on $\langle h_{0k} \rangle \propto \sqrt{\varepsilon_b}$. Thus, for a given initial spectrum h_{0k}, decreasing ε_b by a factor of 4 would effectively reduce $\langle h_{0k} \rangle$ by a factor of 2. From Fig. 5, this would reduce α_b and β_b by only 8% for LEM conditions.

TABLE II. Scaled bubble velocity at $A=1$ from 3D potential flow models. The last two entries, marked with an astersisk, extended the analysis to $A<1$, but with different results.

	$\frac{V_b}{\sqrt{g\lambda_b/2}}$	$\frac{2R_c}{\lambda_b}$	$\frac{V_b}{\sqrt{gR_c}}$
Bubble in cylinder [30–36]			~ 0.5
Hecht, Alon, Shvarts [34]	0.56	1.22	0.51
Inogamov and Abarzhi [37]	0.56	1.02	0.55
Abarzhi [39]	0.59	1.27	0.52
Goncharov* [40]	0.58	1.07	0.56
Sohn* [41]	0.56	1.27	0.50

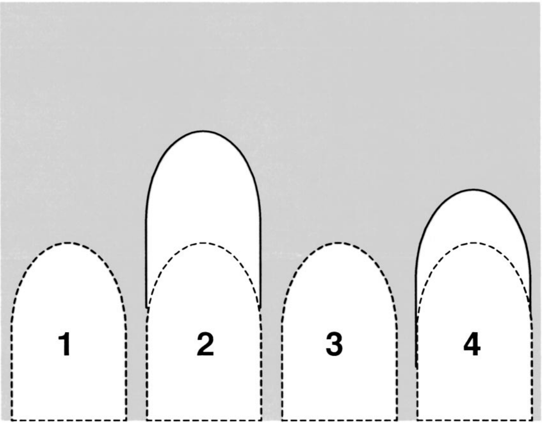

FIG. 7. Schematic of a periodic bubbles array in dashed lines and with bubbles 1 and 4 perturbed forward in solid lines.

ε_b can be estimated by representing the nonlinear wave packet (modes above dashed line in Fig. 3) with a spectrum peaked at k_b and bounded symmetrically by the newly saturated mode k_s, such that $\delta k \sim (k_b - k_s)/2$. This is similar to the bubble distribution in Fig. 6(c) in Oron *et al.* [18]. Then, δk is obtained by identifying k_s at the time that the dominant bubble has k_b, but this must be done self-consistently because the saturation amplitude

$$h_{k_s} \sim \frac{C\pi}{Lk_s^2}\sqrt{\frac{k}{\delta k}} \tag{25}$$

itself depends on the spectral width. Equation (25) resembles the Haan [51] result and is obtained using Eqs. (15) and (17) by assuming $\delta k^2/k^2 \ll 1$.

From self-similarity, the dominant bubble has $k_b = 2\pi/\beta_b h_b$ at a time $t_b\sqrt{2\pi/Ag\beta_b\alpha_b k_b}$. The mode k_s that has just saturated at $t=t_b$ is obtained by combining Eqs. (5) and (25). This yields

$$\sqrt{Ak_s g t_b^2} = \ln\left(\frac{2h_{k_s}}{h_{0k_s}}\right). \tag{26}$$

Using Eqs. (21)–(23), this can be rewritten as

$$\sqrt{\frac{k_b}{4k_s}} = \frac{\ln(2C\sqrt{\pi}/k\langle h_{0k}\rangle) - 1}{\ln(2C\pi\sqrt{k/\delta k}/Lk^2 h_{0k})}, \tag{27}$$

where the right-hand side (RHS) is evaluated at $k=k_s$. Equation (27) has a simple solution for an initial spectrum of the form

$$h_{0k} = \chi/Lk^2 \tag{28}$$

because

$$k\langle h_{0k}\rangle \sim \chi\sqrt{\delta k/\pi k} \tag{29}$$

and the arguments on the right-hand side (RHS) of Eq. (27) are both $\sim 2C\pi/\chi\sqrt{\varepsilon_b}$. Then, for $\chi\sqrt{\varepsilon_b} \ll 2C\pi/e$, the RHS ~ 1 and the solution is $k_s \sim k_b/4$. [This is similar to Fig. 4 in which a packet at mode $n/4$ becomes nonlinear (point) when mode n is dominant.] This result suggests that $dk/k \sim (1-ks/kb)/2 \sim 3/8$, which is consistent with the bubble distribution obtained by Oron *et al.* [18] [Fig. 6(c)].

In order to demonstrate the sensitivity of the model to ε_b and the spectral shape, consider the measured initial spectrum of a glass ICF capsule shown in Fig. 8. h_{0k} (solid line) decreases as k^{-2} until mode 20 and then remains fairly flat out past mode 100. The corresponding value of $k\langle h_{0k}\rangle$ for $\varepsilon_b = 3/8$ is also shown as a dashed line and it is relatively flat only when $h_{0k} \propto k^{-2}$. Physically, this occurs because the number of *e*-foldings required for a wave packet to reach saturation is independent of *k*. For modes >20, $k\langle h_{0k}\rangle$ increases with k because the spectrum exceeds the k^{-2} extrapolation from small *k*. Since the high mode numbers dominate early in time, the initial growth is expected to have $\alpha_b \sim 0.08$ for $k\langle h_{0k}\rangle \sim 0.01$. Later, if the self-similar evolution reaches mode 20, then α_b will remain constant at ~ 0.05 since $k\langle h_{0k}\rangle \sim 0.0004$. When such a value of α_b was used to calibrate a turbulence mix model, the calculation reproduced the observed degradation of neutron yield [67]. If the value of ε_b is reduced by a factor of 4, then the corresponding values of $k\langle h_{0k}\rangle$ would be 50% smaller than the dashed line for this measured spectrum, but the values of α_b would be reduced by <10 %.

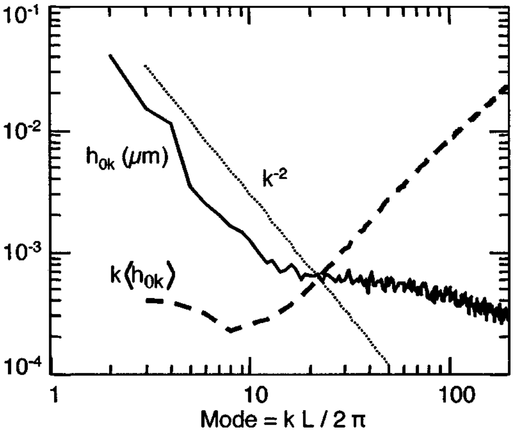

FIG. 8. Measured spectrum (solid) for a glass ICF capsule and effective $k\langle h_{0k}\rangle$ (dashed) for $\varepsilon_b = 3/8$. The dotted line indicates k^{-2} variation.

IV. COMPARISON WITH LEM EXPERIMENTS

A more direct comparison can be made with the planar and incompressible experiments on the LEM. The initial amplitudes are evaluated here by analyzing the early LIF images [12–14] before strong nonlinearities develop. A sample bilevel image taken with a thin laser sheet at 16 ms is shown in Fig. 9(a) over the central 4 cm region ($L=7.3$ cm) for $\rho_h = 1.57$ g/cm^3, $\rho_l = 1.04$ g/cm^3, g $\sim$ 70 g_0 (g_0=Earth's gravity), and $\sigma \sim 4$ dyn/cm. The corresponding interface profile is shown in Fig. 9(b) with a magnified vertical scale and averaged over $\delta x = 0.03$ cm to reduce pixel noise. Its Fourier power spectrum, shown in Fig. 9(c), is dominated ($\sim$80% of energy) by a group of modes centered at $k \sim 38$ cm^{-1} and an rms amplitude $\langle h_k\rangle \sim 0.045$ cm within $\delta k \sim \pm 12$ cm^{-1}. The central wave number can also be obtained by counting bubbles (24 in 4 cm) and from correlation analysis. This data is used to infer the initial rms amplitude $\langle h_{0k}\rangle$ by inverting Eqs. (5) or (19). If modes near $k \sim 38$ cm^{-1} grew exponentially throughout, they would have $\int\Gamma dt \sim 10.4$ *e*-foldings and an amplification of $\exp\int\Gamma dt \sim 16000$. Then, inverting Eq. (5) implies $\langle h_{0k}\rangle \sim 2.7\times10^{-6}$ cm. However, since $k\langle h_k\rangle \sim 1.7$ in Fig. 9, this wave packet has become weakly nonlinear and exceeds Eq. (17) and it is more valid to invert Eq. (19). This can be done using the bubble velocity Eq. (9) while $k\langle h_k\rangle \geq 1$ (assume Fr=0.56 for a maximal effect) and exponential growth Eq. (5) for $k\langle h_k\rangle < 1$. This yields a 50% larger value of $\langle h_{0k}\rangle \sim 3.8\times10^{-6}$ cm. Given this uncertainty, the data implies that $k\langle h_{0k}\rangle \sim (1-1.5)\times10^{-4}$.

A similar analysis of 20 data points under a variety of conditions suggests that the perturbations are seeded by the initial vibrations on the LEM because $k\langle h_{0k}\rangle$ is found to in-

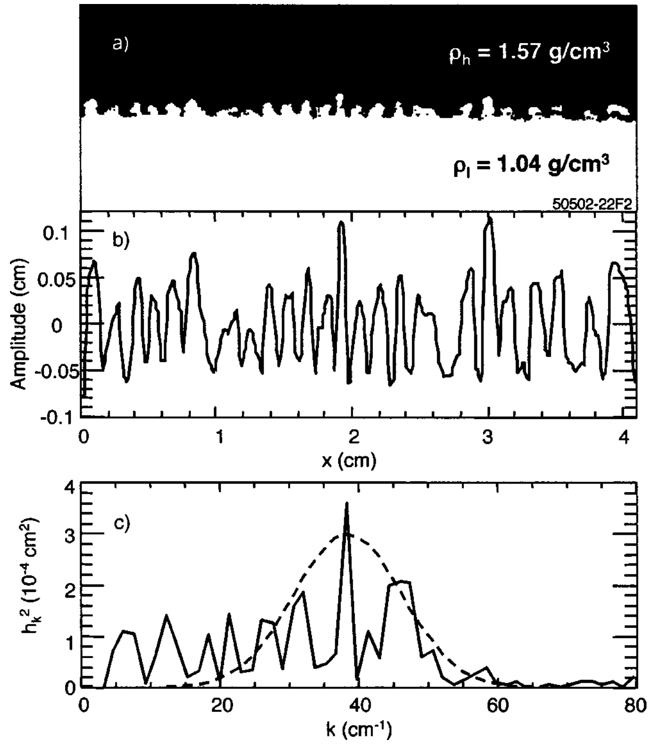

FIG. 9. Analysis of LIF images from the LEM taken at 16 ms to obtain effective initial amplitude. (a) Bilevel image, (b) transverse interface profile, and (c) Fourier power spectrum. The dashed line represents a Gaussian wave packet centered at the dominant mode.

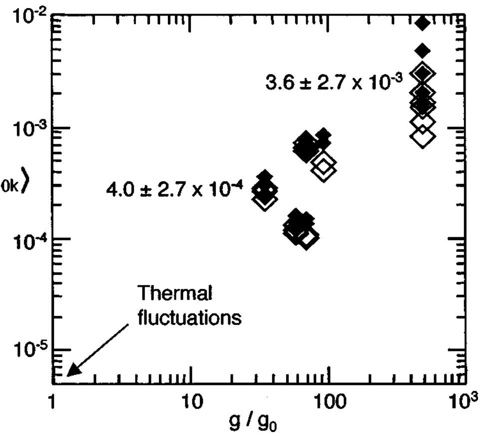

FIG. 10. Inferred initial amplitude on the LEM for various accelerations using the same analysis as in Fig. 9. Open diamonds assume exponential growth [Eq. (4)] throughout and solid diamonds assume the full nonlinear solution [Eq. (19)]. The thermal fluctuations are estimated from Eq. (30). The group at $g/g_0 \sim 30-100$ represents the data used to measure α_b and D_b/h_b and it has an average value of $k\langle h_{0k}\rangle \sim 4.0 \pm 2.7 \times 10^{-4}$.

crease with g as shown in Fig. 10. The open diamonds are obtained assuming exponential growth Eq. (5) and the closed diamonds use Eq. (19) to account for the slight nonlinearity during the final ~1 ms and are 50% higher. In these initial data, the observed wave number is typically $k \sim 25-45\ \mathrm{cm}^{-1}$ and the inferred amplification is $(1-16) \times 10^3$. The results can be clustered into two groups with $k\langle h_{0k}\rangle = (4\pm 2.7)\times 10^{-4}$ for $g \sim (30-100)g_0$ and $k\langle h_{0k}\rangle \sim (3.6\pm 2.7)\times 10^{-3}$ for $g \sim 500\ g_0$. These initial perturbations are indeed small but greatly exceed the thermal fluctuations [51]:

$$h_{0k} = \frac{1}{L}\sqrt{\frac{\kappa_B T}{\delta\rho g_0 + \sigma k^2}}, \tag{30}$$

where κ_B is Boltzmann's constant and T is temperature. The expected rms thermal amplitude is $\langle h_{0k}\rangle \sim \sqrt{\kappa_B T/\sigma} \sim 10^{-7}$ cm with a fastest growing mode of $k_p \sim 50\ \mathrm{cm}^{-1}$. Thus, the thermal fluctuations have $k_p\langle h_{0k}\rangle \sim 5\times 10^{-6}$ and are much smaller than those inferred on the LEM by a factor of g/g_0 and this suggests vibrations as a source. The large scatter in the data may be due to the uncertainty in amplification because a 10% error in Γ translates to a factor of 3 uncertainty in $\langle h_{0k}\rangle$. This would require a 100% uncertainty in σ, which is unlikely because it was measured [13] in situ to 20% using the capillary method. A second source of error may be due to the 30% spread in k in Fig. 9(c) because Γ varies by 10% in this spectral range. This may be mitigated by the fact that the modes become correlated in the nonlinear phase. In addition, the initial spectrum is assumed to be k^{-2} with the same value of $k\langle h_{0k}\rangle$ throughout each experiment. This is consistent with the observations [13,14] that α_b is constant in time for most cases. For these various reasons, our reported values of $k\langle h_{0k}\rangle$ for LEM experiments should be regarded as approximate ~exp(±1) and more direct early time measurements would be useful. This may require laser scattering because the amplitudes are small.

The LEM measurements [12–14] of $\alpha_b \sim 0.05 \pm 10\%$ and $\beta_b \sim 0.55 \pm 25\%$ and (at $A=1$) were obtained with $g \sim (30-100)g_0$ for which $k\langle h_{0k}\rangle \sim 4\pm 2.7\times 10^{-4}$. With these values, it can be seen in Fig. 5 that the present model is able to describe the LEM observations of α_b and β_b with $C \sim 0.95$ (solid line). The data is inconsistent with the $C \sim 0.56$ (dashed line) expected from potential flow for a square lattice [34] even with the large experimental uncertainty in $k\langle h_{0k}\rangle$ because α_b and β_b vary differently with C. With $C=0.56$, the agreement for α_b would be improved by increasing $k\langle h_{0k}\rangle$ tenfold but it would be degraded for β_b and vice versa if $k\langle h_{0k}\rangle$ is decreased.

The value of Fr can be obtained independent of this model by analyzing individual bubbles in RT experiments [21–24,43,44]. This is exemplified here with a bilevel LIF image in Fig. 11 for the same conditions of Fig. 9 but at $gt^2/2 \sim 90$ cm. The five bubbles comprising the front have $D_b \sim 0.6\pm 0.23$ cm. Inserting this into Eq. (2) with their velocity taken as $V_b \sim 2\alpha_b Agt$ yields $\mathrm{Fr} \sim 0.81 \pm 0.16$. D_b was also measured at different Atwood numbers with LIF and backlit photography [14]. Applying the above analysis to this data yields the solid points in Fig. 12 which have an average value of $\mathrm{Fr} \sim 0.88 \pm 0.15$. This value is ~20% smaller than obtained in a similar way by Lewis [43] and Glimm [21,22] and Li [41] (open circles) for the "rocket rig" experiments [7,8]. Scorer [35] analyzed plumes and found $\mathrm{Fr} \sim 1.2$ when he accounted for the density dilution as they spread. The

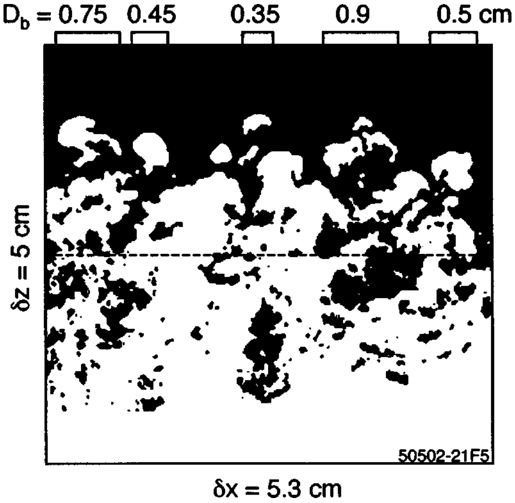

FIG. 11. Bilevel image from LIF for the same conditions as in Fig. 9 at $gt^2 \sim 90$ cm. The black region has $\rho_h \sim 1.57$ gm/cm^3 and the white region has $\rho_l \sim 1.04$ gm/cm^3. The diameters of five leading bubbles D_b are indicated in cm.

values of Fr inferred from the LEM may be low because such a dilution due to entrainment is not taken into account. The LIF images [13,14] like those in Fig. 11 exhibit some entrainment but the laser beam is too thick to quantify this accurately.

The LEM data [14] is compared with the present model over a comprehensive range of A in Fig. 13. The lines from the model are obtained with $k\langle h_{0k}\rangle \sim 4\times 10^{-4}$ but there is a ±70% uncertainty in $k\langle h_{0k}\rangle$. α_b is compared directly in (a) but the self-similarity ratio in (b) is represented by D_b/h_b since that is what was measured on the LEM. However, the model is based on λ_b/h_b and a transformation between D_b and λ_b is required to relate Eqs. (2), (8), and (9) as discussed in Sec. II A. Thus two model calculations are shown in Fig. 13. The dashed lines are with a constant $C=0.95$ in Eq. (9) or, equivalently, with Fr=0.95 in Eq. (2) and assuming the Daly hypothesis $D_b=\lambda_b(1+A)/2$. The solid lines are with $C=0.82\sqrt{2/(1+A)}$ in Eq. (9) or, equivalently, with Fr=0.82 in Eq. (2) and assuming $D_b=\lambda_b$. The first case obtains a constant $\alpha_b \sim 0.052$ and a linearly increasing D_b/h_b with A. In the second calculation, α_b decreases slightly with A whereas D_b/h_b increases slightly with A. Both are consistent with the data within the experimental scatter.

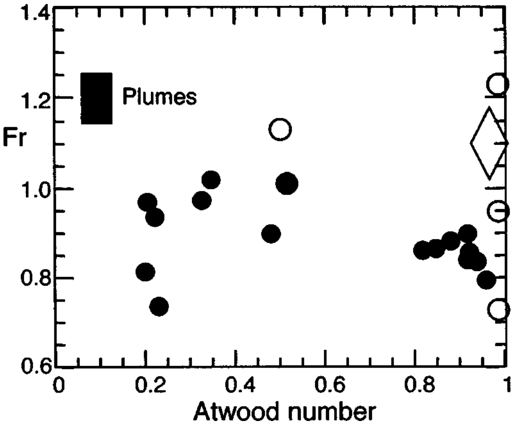

FIG. 12. Fr obtained by analyzing individual bubbles in RT experiments using Eq. (2): ●, LEM [14]; ○, Rocket rig [21]; ◇, Lewis [40]; ■, Plumes [32].

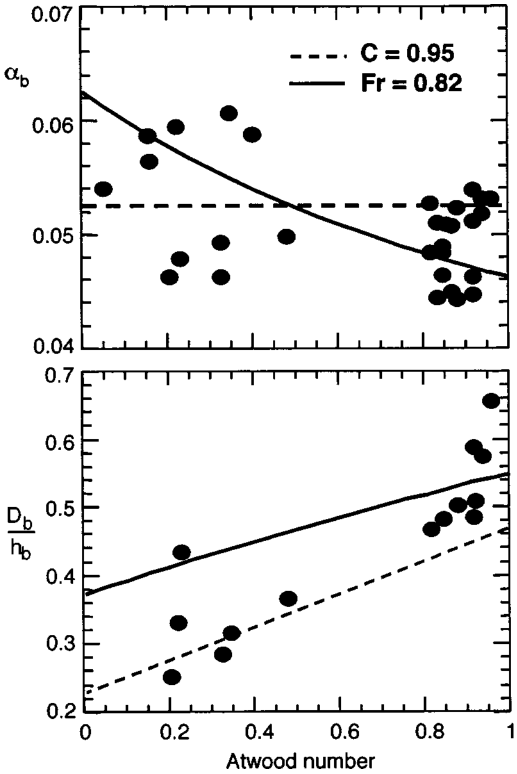

FIG. 13. Variation of α_b and D_b/h_b vs A for LEM measurements [14] (points) and model with $C=0.95$ (dashed) and $C=0.82$ (solid).

In both cases, the experimental data show that the leading RT bubbles have an Fr that exceeds that of a single PERIODIC ARRAY of bubbles, either directly in Fig. 12 and cited references or within the context of this model in Figs. 5 and 13. This realization caused Glimm and collaborators [21–24] to suggest an envelope instability in which bubbles in a chaotic array are catapulted by their neighbors. They proposed augmenting the single bubble velocity with the corresponding velocity for a modulated envelope at $2\lambda_b$ and obtained $\alpha_b \sim 0.05$–0.06 with $D_b/h_b \sim 1/3$. However, as discussed in Sec. III A, this may not be necessary because any bubble that is perturbed forward will behave more like an unbounded plume with Fr ~ 1 than a bounded periodic array with Fr ~ 1/2. Oron *et al.* [18] tried to compensate for the small Fr of a periodic array by increasing the bubble merger rate, but this made their $\lambda_b/h_b \sim 1$, which is ~3× larger than observed in Fig. 13.

V. AUGMENTATION OF LONG-WAVELENGTH PERTURBATIONS BY MODE COUPLING

In many experiments and simulations, the growth rate α_b is reported near the end of the time domain in order to minimize any initial transients. In this limit, the value of α_b is determined primarily by the long-wavelength initial perturbations because $h_b \sim L/2$ and they can be augemented by the nonlinear mode coupling of the most unstable modes at short wavelengths. This is expected to reduce the sensitivity of α_b on initial conditions [4,46] and it is important in most multimode NS [15–20] because they have been initialized with perturbations primarily in a high wavenumber band $k_0 \pm \delta k_0$. In such a case, low-k modes $k \leqslant \delta k_0$ are produced through the nonlinear coupling of the more unstable high-k modes that have saturated. This effect can be incorporated into the present model by calculating the low-k products using Eq. (15) from Ref. [52]:

$$H_k^2 \sim A^2k^2\frac{L^2}{2\pi}\int_{k_0-\delta k_0}^{k_0+\delta k_0} dk'k'h_{k'}^4, \tag{31}$$

where (capital) H_k is the mode coupling product. The parent waves near k_0 saturate first at a time given by Eq. (18) and an amplitude given by Eq. (25) so that

$$H_k^2 \sim A^2k^2\frac{C^4\pi^3}{L^2k_0^6}\frac{k_0}{\delta k_0}. \tag{32}$$

Using Eq. (15), the amplitude of the low-k wave packet is then

$$\langle H_k\rangle \sim C^2\pi A\frac{k^2}{k_0^3}. \tag{33}$$

This amplitude is generated by mode coupling after the most unstable modes have become nonlinear, i.e., for $t > t_{NL}(k_0)$. However, to incorporate the mode coupling product into the present model, it is first necessary to compensate for the equivalent exponential growth from 0 to $t_{NL}(k_0)$. Thus, the equivalent initial amplitude due to mode coupling is obtained by inverting Eq. (5) with $\exp[\sqrt{Akg}t_{\mathrm{NL}}(k_0)]$. This yields

$$k\langle H_{0k}\rangle \sim C^2\pi A\frac{k^3}{k_0^3}\left(\frac{k_0\langle h_{0k}(k=k_0)\rangle}{C\sqrt{\pi}}\right)^{\sqrt{k/k_0}}. \tag{34}$$

Typically, the dominant term is k^3/k_0^3 and the term in parenthesis is of order 20–50%. Haan [52] suggests adding the ambient and mode coupling amplitudes in quadrature as

$$\langle \eta_{0k}\rangle = (\langle h_{0k}\rangle^2 + \langle H_{0k}\rangle^2)^{1/2}. \tag{35}$$

η_{0k} depends on both the amplitude and spectral shape of the initial perturbations as will be exemplified below for two spectra: one that decreases with k given by Eq. (28) and another that peaks at a finite k_0 like those used in the NS.

For a broad spectrum that decreases smoothly with k, the initial saturation occurs for modes near the peak growth rate so that $k_0 \Rightarrow k_p$ and $k\langle H_{0k}\rangle$ depends on k/k_p. This is exemplified in Fig. 14 for the spectrum of Eq. (28) where $k\langle h_{0k}\rangle \propto \chi$. When the amplitude of the ambient low-k modes $\langle h_{0k}\rangle$ exceeds that of the initially saturated modes $\propto C/k_p$, mode coupling is not important and $k\langle \eta_{0k}\rangle$ depends only on $k\langle h_{0k}\rangle$. From Eqs. (34) and (35), mode coupling dominates when $\langle h_{0k}\rangle < \langle H_{0k}\rangle \sim 0.1k^2/k_p^3$ and this sets a lower bound on $k\langle \eta_{0k}\rangle$ that depends on k^3/k_p^3 rather than $k\langle h_{0k}\rangle$. Then, if α_b is determined from the total amplitude $k\langle \eta_{0k}\rangle$, as shown in Fig. 14(b) α_b approaches a lower bound that is insensitive to the initial amplitude. In fact, the minimum α_b depends primarily on k/k_p and this translates to an asymptotic dependence of α_b on Reynolds number for a system in which k_p is determined by viscosity and $k \sim 2\pi/L$.

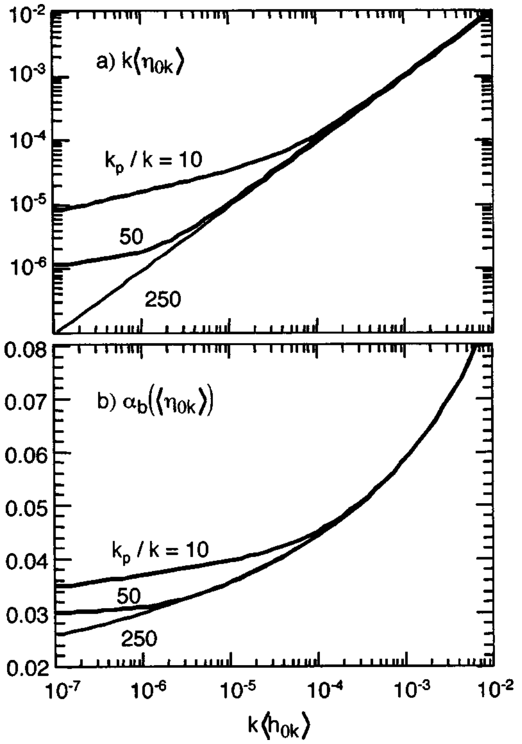

FIG. 14. The total effective initial amplitude $k\langle \eta_{0k}\rangle$ including the mode coupling product using Eqs. (34) and (35). The acceleration constant α_b is obtained by substituting $k\langle \eta_{0k}\rangle$ for $k\langle h_{0k}\rangle$ in Eq. (22).

Since this lower bound of α_b is thought to be its most fundamental value because it is most insensitive to initial conditions, the NS were designed to accentuate mode coupling. This is done with initial perturbations peaked at a finite k_0 and deficient at low k. Some high resolution 3D NS are summarized in Table III and most are initialized robustly with modes numbers $n_0 > 10$ that are nearly nonlinear, i.e., $k_0\langle h_{0k_0}\rangle \sim 0.1-1$. When the initial spectrum is a shell in k space [16], the low-k modes are produced entirely by mode coupling and the analysis differs slightly from that associated with Fig. 14. A crude attempt at evaluating mode coupling is shown in Fig. 15. For the annular spectra, the low-k product $k\langle H_{0k}\rangle$ is evaluated by Eq. (34) with $C = 0.95$ and $A = 0.5$. The NS have $A = 0.5$ except that of Young *et al.* [20] which uses the Boussinesq approximation and is most valid for $A \ll 1$. The most important uncertainty in evaluating these NS is identifying which low-k mode dominates at the late time when α_b is determined. The points in Fig. 15 are obtained by assuming the lowest mode $k = 2\pi/L$ as a limiting case. This seems reasonable since the more detailed calculation by Haan [52] shows in his Fig. 3 that the mode coupling product increases only (2–3) fold from mode 1 to 5. However, these values of $k\langle H_{0k}\rangle$ should be regarded as minimum values (see error bars) except for Ref. [20] for A $\ll$ 1. Even with this large uncertainty, the solid points exhibit a slow increase in

TABLE III. Summary of recent high resolution NS of multimode RT: average initial modes numbers, rms initial amplitude, and acceleration constant, all done with $A=0.5$ except [20], which uses the Boussinesq approximation and is most valid for $A \ll 1$. NS using front tracking are designated with FT.

Simulation/zoning	n_0	$k_0\langle h_{0k_0}\rangle$	α_b
(1) Youngs [16]			
$160\times160\times270$	30	0.08	0.03
(2) Cook and Dimotakis [19]			
$256\times256\times512$			
Case A	4	0.3	0.05–0.08
Case B	9	0.6	0.03–0.05
Case C	13	0.9	0.02–0.03
(3) Young *et al.* [20]			
$256\times256\times512$	13	0.9	0.03
(4) Glimm *et al.* [17]			
$112\times112\times224$	12	0.4	0.05
	12	0.4	0.08 FT
(5) Oron *et al.* [18]			
$80\times80\times80$	$\sqrt{300}$		0.05 FT

α_b with $k\langle H_{0k}\rangle$ similar to the present model (lines) with $C=0.95$ (solid) and 0.56 (dashed). The 3 cases of Cook and Dimotakis [19] are interesting because they have the same initial rms amplitude $\langle h_{0k_0}\rangle \sim 0.01L$, yet they show an increase in α_b as the initial peak n_0 is reduced. The solid points favor the smaller value of C, but this may be due to the large species diffusion [16]. Indeed, the open circles representing the NS using front-tracking exhibit a larger value of α_b. (Please note that $k_0\langle h_{0k_0}\rangle$ was not reported in Ref. [18] and was taken as 0.5 here since they initialize with bubbles). It is thought that front-tracking inhibits numerical diffusion which can dilute the bubbles and reduce their effective buoyancy. However, entrainment [28,29] may be fundamental to the turbulent RT instability and can be inhibited by an aggressive front-tracking scheme or with a high surface tension [14]. Clearly, more NS are needed to clarify these issues but with precisely reported initial conditions and self-similarity parameter β_b.

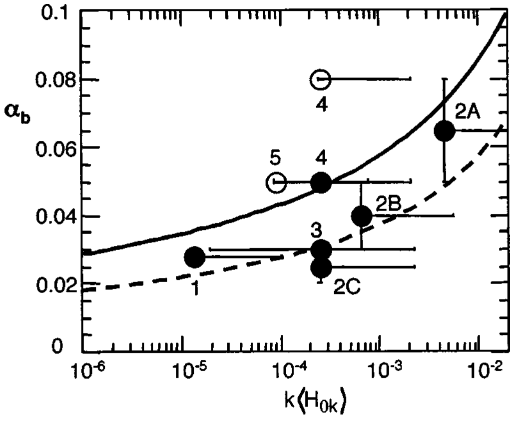

FIG. 15. The effect of mode coupling for an annular spectrum like the NS in Table III. Here the mode-coupling product $k\langle H_{0k}\rangle$ is evaluated using Eq. (34) assuming $k=2\pi/L$ for each NS in Table III (points with designation in Table III). The lines are obtained by substituting $k\langle \eta_{0k}\rangle$ for $k\langle h_{0k}\rangle$ in Eq. (22) for $C=0.95$ (solid) and 0.56 (dashed).

VI. SUMMARY AND DISCUSSION

A model has been presented here to quantify the effect of initial conditions on the bubble acceleration constant α_b and the self-similarity ratio β_b for arbitrary Atwood number. The model has two free parameters related to the terminal velocity (Fr or C) and the spectral distribution (ε_b) of the dominant bubbles. The coefficients are determined from numerical simulations and experiments. In particular, the initial perturbations in the LEM experiments are estimated by analyzing the early time LIF images and Fr is determined from individual bubble dynamics in late time images. It is found that RT bubbles have $\mathrm{Fr}\sim1$ more like plumes or unbounded bubbles than a periodic bubble array in which $\mathrm{Fr}\sim1/2$. The model finds that $\alpha_b \propto C$ and $\beta_b \propto 1/C$ and that both increase logarithmically with the initial perturbation amplitude. The weak logarithmic dependence may be responsible for the small variation in the measured values of $\alpha_b \sim 0.04-0.08$ since such a variation in α_b corresponds to a factor of 100 variation in initial amplitude. The effect of mode coupling is also evaluated and found to reduce the sensitivity of α_b on the initial perturbations when the long wavelength modes are smaller than the saturation amplitude of the most unstable modes. The model and results are described in more detail in the following.

The model is based on Birkhoff's [3] adaptation of Fermi's single mode solution [32] of the RT instability at $A=1$. The exponential growth at small amplitude is taken to transition to the bubble terminal velocity at large amplitude with a continuous slope and amplitude. This occurs near $h_k \sim 1/k$ when the growth rate is classical. To describe the multimode case, Birkhoff [3] allowed the dominant mode in the nonlinear solution h_k to vary by setting $\partial h_k/\partial\lambda=0$. This yielded self-similar solutions with $\alpha_b\sim0.12$ and $\beta_b\sim1.0$ for an assumed initial perturbation $h_{0k}\sim10^{-3}/k$, within a factor of 2 of measurements made decades later.

The present model makes two simple extensions to Birkhoff's analysis to arbitrary A and initial perturbations. The extension to all A depends on how the bubble terminal velocity varies with A. Since the result of Alon *et al.* [26] and Goncharov [40] [Eq. (8)] differs from that of Sohn [41] and Glimm and Li [21] [Eq. (9)] by a factor of $\sqrt{(1+A)/2}$, the velocity was taken to have the form of Eq. (9) but with a constant C that can very slowly with A to accommodate Eq. (8). Both formulations can be obtained from the classic result Eq. (2) by changing the relation between D_b and λ_b, and they are consistent with 3D simulations (Fig. 1) within their scatter. The second extension is related to how a single mode solution can be applied to the more realistic multimode environment. This was done here using the model of DeNeef [60] for the beam-plasma instability and Haan [51,52] for the RT instability in which the rms amplitude of a multimode wave packet is found to evolve just like that of a single mode until an autocorrelation (resolution) time after the onset of nonlinearity. This implies that individual modes saturate at smaller amplitudes $h_k \sim 1/k^2L$ than suggested by Birkhoff $h_k \sim 1/k$ and that the simplest self-similar solution occurs for initial perturbations of the form $h_{0k} \sim 1/k^2$ as suggested by Inogamov [5,6] rather than $h_{0k} \sim 1/k$ suggested by Birkhoff [3]. This mode suppression was measured directly in a beam-plasma experiment [61].

The most important model parameter C determines the terminal bubble velocity as defined by Eq. (9) and it can vary slowly with A to accommodate Eq. (8). C can be related to the more basic constant Fr in Eq. (2) on a physical basis by defining a relation between D_b and λ_b [Eq. (11)], but it may also absorb additional uncertainties in this model. The model is able to describe the LEM data with $C \sim 0.95$ or $\mathrm{Fr} \sim 0.8$ which is similar to that obtained in Fig. 12 by analyzing individual RT bubbles [43,21,22,14,24]. This is important because using the anticipated value of $\mathrm{Fr} \sim 1/\sqrt{\pi}$ for a square periodic bubble array and the observed $D_b/h_b \sim 0.55\rho_h/\Sigma\rho$ in Eq. (3) yields an $\alpha_b \sim 0.022$ that is smaller than observed. This led Glimm and collaborators [21–24] to suggest an envelope instability that augments the Fr in a chaotic RT bubble front and obtained $\alpha_b \sim 0.05-0.06$ and $D_b/h_b \sim 1/3$ independent of A. Others [23,24,18] have tried to compensate for the small Fr of a periodic array by increasing the merger rate, but this makes $\lambda_b/h_b \sim 1$ in 3D [18] which is $\sim 3\times$ larger than observed (Fig. 13). These results suggest that RT bubbles behave as a chaotic array with $\mathrm{Fr} \sim 1$ and $D_b/h_b \sim 1/3-1/2$ rather than a periodic array with $\mathrm{Fr} \sim 0.56$ and $D_b/h_b \sim 1$.

The second model parameter ε_b describes the effective spectral width of the dominant bubbles and is used to obtain $k\langle h_{0k}\rangle$ from the measured initial spectrum. As such, α_b and β_b depend only logarithmically on $\sqrt{\varepsilon_b}$. By calculating the just saturated mode k_s relative to the dominant mode k_b, we estimate $\varepsilon_b \sim 3/8$ which is consistent with the spectral width obtained in a 3D bubble merger model [18].

The present model is able to describe the LEM measurements [12–14] of α_b and β_b with $C \sim 0.95$ as shown in Figs. 5 and 13. The initial amplitude in the LEM experiments is obtained from early-time LIF images taken when the perturbations are barely nonlinear and these are projected back to $t=0$ using the well known exponential growth. The perturbations are found to exceed the thermal fluctuations in proportion to g as seen in Fig. 10 and this suggests that they are excited in transit. For the Atwood variation experiments with $g(30-100)g_0$, it was found that $k\langle h_{0k}\rangle = (4 \pm 2.7) \times 10^{-4}$ in the range $k \sim 25-45\ \mathrm{cm}^{-1}$. This value is used at all wavelengths which assumes that the initial spectrum varies as k^{-2}, but this should be measured in future experiments. However, by analyzing individual bubbles in RT experiments, it is clear that they have $\mathrm{Fr} \sim 0.8-1.2$ as indicated in Refs. [43,21,22,14,24] in Table I and Fig. 12 here. This exceeds the $\mathrm{Fr} \sim 0.56$ for a periodic array in Table II [34,37–41] but it is comparable to the $\mathrm{Fr} \sim 1.2$ for plumes [36].

The present model is also compared with published multimode NS summarized in Table III. Since the NS had an initial spectrum peaked at a finite k and devoid of low-k modes that dominate asymptotically when α_b is typically measured, it is necessary to evaluate the generation or augmentation of long wavelenth perturbations by mode coupling. This was done using Haan's formulation [52] and the results depend on the effective spectral width $\delta k \sim 3/8k$. The contribution of mode coupling is found to be important when the product waves from saturated high-k modes exceed the ambient perturbations at low k. As shown in Fig. 14, the net effect of mode coupling is to produce a lower bound in α_b at small initial amplitude that is insensitive to the initial conditions. The present model is consistent with previous NS, but since their initial conditions were somewhat unclear and more complex than $h_{0k} \sim 1/k^2$, the results could not distinguish between $C \sim 0.56$ and 0.95. More 3D NS with well specified initial conditions are required to clarify these issues. It should be repeated that the mode-coupling contribution described here is not a general theory of mode coupling since it does not describe the usual progression to longer wavelength by a cascading process. The latter is done better by merger models [21–26].

ACKNOWLEDGMENTS

I would to like to express my gratitude to David Youngs, Karnig Mikaelian, Praveen Ramaprabhu, Malcolm Andrews and Steve Haan for many useful discussions, Steve Weber for the reproduction of Fig. 3 from Ref. [26], and Marilyn Schneider for contributing to the LEM experiments. This work was performed under the auspices of the U.S. Department of Energy by Los Alamos National Laboratory under Contract No. W-7405-ENG-36 and Lawrence Livermore National Laboratory under Contract No. W-7405-ENG-48.

---

[1] Lord Rayleigh, *Scientific Papers II* (Cambridge University Press, Cambridge, England, 1900), p. 200.
[2] G. I. Taylor, Proc. R. Soc. London, Ser. A **201**, 192 (1950).
[3] G. Birkhoff, University of California, Report No. LA-1862, 1955.
[4] Catherine Cherfils and Karnig O. Mikaelian, Phys. Fluids **8**, 522 (1996).
[5] N. A. Inogamov, Sov. Tech. Phys. Lett. **4**, 299 (1978).
[6] N. A. Inogamov *et al.* in *Proceedings of the Third International Workshop Phys Comp. Turbulent Mixing*, edited by R. Dautray (Commissariat Energie Atomique, Cesta, France, 1991), p. 409.
[7] K. I. Read, Physica D **12**, 45 (1984).
[8] D. L. Youngs, Physica D **37**, 270 (1989).
[9] M. J. Andrews and D. B. Spalding, Phys. Fluids A **2**, 922 (1990).
[10] Yu. A. Kucherenko, L. I. Shibarshov, V. I. Chitaikin, S. I. Balabin, and A. P. Pylaev, in *Proceedings of the Third Inter-*

national Workshop Phys. Comp. Turbulent Mixing (Ref. [6]), p. 427.
[11] P. F. Linden, J. M. Redondo, and D. L. Youngs, J. Fluid Mech. **265**, 97 (1994).
[12] Guy Dimonte and M. Schneider, Phys. Rev. E **54**, 3740 (1996).
[13] M. Schneider, Guy Dimonte, and B. Remington, Phys. Rev. Lett. **80**, 3507 (1998).
[14] Guy Dimonte and M. Schneider, Phys. Fluids **12**, 304 (2000).
[15] D. L. Youngs, Phys. Fluids A **3**, 1312 (1991).
[16] D. L. Youngs, Laser Part. Beams **12**, 725 (1994).
[17] J. Glimm, J. W. Grove, X. L. Li, W. Oh, and D. H. Sharp, J. Comput. Phys. **169**, 652 (2001).
[18] D. Oron, L. Arazi, D. Kartoon, A. Rikanati, U. Alon, and D. Shvarts, Phys. Plasmas **8**, 2883 (2001).
[19] A. W. Cook and P. E. Dimotakis, J. Fluid Mech. **443**, 69 (2001).
[20] Yuan-nan Young, H. Tufo, A. Dubey, and R. Rosner, J. Fluid Mech. **447**, 377 (2001).
[21] J. Glimm and X. L. Li, Phys. Fluids **31**, 2077 (1988).
[22] J. Glimm, X. L. Li, R. Menikoff, D. H. Sharp, and Q. Zhang, Phys. Fluids A **2**, 2046 (1990).
[23] J. Glimm and D. Sharp, Phys. Rev. Lett. **64**, 2137 (1990).
[24] B. Cheng, J. Glimm, and D. Sharp, Chaos **12**, 267 (2002).
[25] D. Shvarts, U. Alon, D. Ofer, R. L. McCrory, and C. P. Verdon, Phys. Plasmas **2**, 2465 (1995).
[26] U. Alon, J. Hecht, D. Ofer, and D. Shvarts, Phys. Rev. Lett. **74**, 534 (1995).
[27] D. L. Youngs, AIAA Pap. **2003**, 4102 (2003).
[28] E. George, J. Glimm, X. L. Li, A. Marchese, and Z. L. Xu, Proc. Natl. Acad. Sci. U.S.A. **99**, 2587 (2002).
[29] Guy Dimonte *et al.* (unpublished).
[30] D. T. Dumitrescu, Z. Angew. Math. Mech. **23**, 139 (1943).
[31] R. M. Davies and G. I. Taylor, Proc. R. Soc. London, Ser. A **200**, 375 (1950).
[32] D. Layzer, Astrophys. J. **122**, 1 (1955).
[33] H. J. Kull, Phys. Rep. **206**, 197 (1991).
[34] J. Hecht, U. Alon, and D. Shvarts, Phys. Fluids **6**, 4019 (1994).
[35] R. S. Scorer, J. Fluid Mech. **2**, 583 (1957).
[36] R. Collins, J. Fluid Mech. **28**, 97 (1967).
[37] N. A. Inogamov and S. I. Abarzhi, Physica D **87**, 339 (1995).
[38] Karnig O. Mikaelian, Phys. Rev. Lett. **80**, 508 (1998).
[39] S. I. Abarzhi, Phys. Rev. E **59**, 1729 (1999).
[40] V. N. Goncharov, Phys. Rev. Lett. **88**, 134502 (2002).
[41] Sung-lk Sohn, Phys. Rev. E **67**, 026301 (2003).
[42] Karnig O. Mikaelian, Phys. Rev. E **67**, 026319 (2003).
[43] D. J. Lewis, Proc. R. Soc. London, Ser. A **202**, 81 (1950).
[44] X. L. Li, Phys. Fluids **8**, 336 (1996).
[45] G. Tryggvason and S. O. Unverdi, Phys. Fluids A **2**, 656 (1990).
[46] X. L. Li, Phys. Fluids A **5**, 1904 (1993).
[47] X. L. Li, B. X. Jin, and J. Glimm, J. Comput. Phys. **126**, 343 (1996).
[48] J. Hecht, D. Offer, U. Alon, D. Shvarts, S. A. Orszag, and R. L. McCrory, Laser Part. Beams **13**, 423 (1995).
[49] X. He, R. Zhang, S. Chen, and G. Doolen, Phys. Fluids **11**, 1143 (1999).
[50] Alan Calder *et al.*, Astrophys. J., Suppl. Ser. **143**, 201 (2002).
[51] S. W. Haan, Phys. Rev. A **39**, 5812 (1989).
[52] S. W. Haan, Phys. Fluids B **3**, 2349 (1991).
[53] V. A. Andronov, S. M. Bakhrakh, V. N. Mokhov, V. V. Nikiforov, and A. V. Pevnitskii, JETP Lett. **29**, 56 (1979).
[54] S. Gauthier and M. Bonnet, Phys. Fluids A **2**, 592 (1990).
[55] J. C. Hanson, P. A. Rosen, T. J. Goldsack, K Oades, P. Fieldhouse, N. Cowperthwaite, D. L. Youngs, N. Mawhinney, and A. J. Baxter, Laser Part. Beams **8**, 51 (1990).
[56] J. Glimm, D. Saltz, and D. H. Sharp, Phys. Rev. Lett. **80**, 712 (1998).
[57] J. D. Ramshaw, Phys. Rev. E **58**, 5834 (1998).
[58] Guy Dimonte, Phys. Plasmas **7**, 2255 (2000).
[59] V. E. Neuvazhaev and V. G. Yakovlev, J. Appl. Mech. Tech. Phys. **42**, 572 (2001).
[60] C. P. DeNeef, J. H. Malmberg, and T. M. O'Neil, Phys. Rev. Lett. **30**, 1032 (1973); Peter DeNeef, Phys. Fluids **18**, 1209 (1975).
[61] Guy Dimonte, Phys. Fluids **25**, 604 (1982).
[62] S. Chandrasekhar, *Hydrodynamic and Hydromagnetic Stability* (Oxford University Press, Oxford, 1961).
[63] S. Bodner, Phys. Rev. Lett. **33**, 761 (1974).
[64] H. Takabe *et al.*, Phys. Fluids **28**, 3676 (1985).
[65] B. J. Daly, Phys. Fluids **10**, 297 (1967).
[66] R. D. Blevins, *Applied Fluid Dynamics Handbook* (Van Nostrand Reinhold, New York, 1984), p. 332.
[67] Guy Dimonte, R. Turner, O. Landen, R. Tipton, P. Amendt, J. Colvin, K. Mikaelian, O. Jones, and R. Wallace, Bull. Am. Phys. Soc. **46**, 141 (2001).